Nanoscale

PAPER

View Article Online
View Journal | View Issue

Cite this: *Nanoscale*, 2025, **17**, 9337

Synthesis of intrinsically sodium intercalated ultra-thin layered MnO_2 and its ionic charge transport†

Amir Parsi, [a] Abdulsalam Aji Suleiman,‡[a] Mohammadali Razeghi, §[a] Doruk Pehlivanoğlu, [a] Oğuzhan Oğuz,[a] Uğur Başçı,[b] Hafiz Muhammad Shakir,[b] Emine Yegin[a] and T. Serkan Kasırga *[a]

Ionic motion at the interlamellar space in layered materials can provide superior properties in electrochemical energy storage, neuromorphic computing, and ion-mediated charge transport. Herein, we demonstrate the synthesis of ultra-thin, single-crystalline MnO_2 nanosheets intercalated with Na^+ ions during molten-salt-assisted chemical vapor deposition. Unlike the post-intercalation of alkali ions into a host material, this method facilitates spontaneous Na^+ intercalation during crystal formation, yielding highly ordered layered δ-MnO_2 (birnessite-type phase) with structural stability. Our in-depth studies, including X-ray diffraction, Raman spectroscopy, and transmission electron microscopy, on the as-synthesized Na-MnO_2 crystals elucidate the crystal properties and highlight that ambient moisture significantly affects the movement of ions and improves their electrochemical stability. Furthermore, we used two-terminal devices of Na-MnO_2 crystals to show hysteretic behavior due to the ionic charge transport mechanisms, making them highly suitable for neuromorphic applications.

Received 19th December 2024,
Accepted 7th March 2025

DOI: 10.1039/d4nr05342g

rsc.li/nanoscale

1. Introduction

Ion-mediated mass and charge transport in layered materials offers new avenues in electrochemical energy storage and mixed ion–electron conductor devices for neuromorphic applications.[1,2] This ionic transport can be achieved *via* either extrinsically or intrinsically intercalated interlamellar guest ions into a host material. In the case of intrinsic ionic crystals, the interlamellar ions are spontaneously intercalated during the formation of the crystal, whereas in the extrinsic case, ions are electrically or diffusively intercalated across the layers of the host material.[3] Extrinsic ionic crystals can offer flexibility in creating various composite structures. As an example, previously, high-performance supercapacitor application through intercalating various guest ions such as H^+, Li^+, and Na^+ into MoS_2 and improved hydrogen evolution reactions in ion-intercalated WS_2 has been demonstrated.[4–7] However, wrinkling and distortion of the host crystal after the intercalation limit the usability of extrinsic doping.[4] Moreover, extrinsic doping of crystals is a slow process, and for planar devices, it is challenging to achieve large-area uniform doping within industrially feasible durations. Intrinsically ion-doped layered materials are superior alternatives to extrinsically doped ionic layered materials as interlamellar doping is performed spontaneously during the crystal synthesis. Many steps that involve electrochemical doping and wet ion chemistry are removed from device fabrication.

One important example of an intrinsically ion-intercalated layered material is manganese dioxide, known as δ-MnO_2 (also referred to as birnessite).[8–11] δ-MnO_2 has garnered significant attention in recent decades as a promising material for energy storage[10,12,13] and catalysis[14,15] owing to its affordability, environmental friendliness,[13,16] and unique layered structure, which facilitates ion diffusion. Birnessite has been synthesized by various methods, including simple reduction, thermal decomposition, electrodeposition, co-precipitation, sol–gel, and hydrothermal methods.[17] The layered arrangement of δ-MnO_2 allows for the accommodation of water molecules and alkali cations such as Li^+, Na^+, and K^+ in the interlamellar space. These ions alleviate the electrostatic repulsion between the layers of MnO_2, thereby enhancing the overall structural stability.[18–22]

A novel approach for synthesizing δ-MnO_2 is the molten-salt-assisted chemical vapor deposition (CVD) technique. By lowering the melting temperature of precursors, this method enhances reaction kinetics, allowing precise control over

[a]*Bilkent University UNAM – Institute of Materials Science and Nanotechnology, Ankara 06800, Türkiye. E-mail: kasirga@unam.bilkent.edu.tr*
[b]*Department of Physics, Bilkent University, Ankara 06800, Türkiye*

†Electronic supplementary information (ESI) available. See DOI: **https://doi.org/10.1039/d4nr05342g**

‡Current Address: Engineering Fundamental Science Department, Sivas University of Science and Technology, Sivas 58010, Türkiye.
§Current Address: IMCN/NAPS, Université Catholique de Louvain (UCLouvain), 1348, Louvain-la-Neuve, Belgium.

crystal growth and ensuring high uniformity in the resulting crystals. Compared to conventional synthesis methods for δ-MnO_2, molten-salt-assisted CVD offers superior crystalline quality.[19] Beyond its advantages in crystal growth, this technique also introduces a breakthrough in interlamellar doping strategies. Unlike conventional methods used to extrinsically dope layered materials, this approach enables spontaneous interlamellar intercalation of guest ions during crystal growth, resulting in large-area uniform doping.[23–25] By combining high crystallinity with efficient, one-step spontaneous doping, the molten-salt-assisted CVD technique can represent a significant advancement in the synthesis and engineering of δ-MnO_2 and related materials.

Until recently, no large-area single crystalline samples were available, and a fundamental understanding of charge transport mechanisms across these single crystalline samples was lacking. Our previous work demonstrated that δ-MnO_2 can be spontaneously intercalated with K^+ to obtain ultra-thin K-MnO_2 single-crystals *via* molten-salt-assisted CVD[19] and K-MnO_2 crystals can be used to mimic synaptic responses and achieve long-term potentiation and depression properties. Exploring a similar approach with other alkali ions for enhancing the performance of δ-MnO_2 is highly promising. The intercalation of layered MnO_2 with Na^+ may offer key advantages for artificial synaptic devices by leveraging the biological relevance of sodium ions, which play a crucial role in neuronal signal transduction.[26] The smaller ionic radius of Na^+ (1.02 Å) than that of K^+ (1.38 Å) may allow for more efficient ionic transport and intercalation within the MnO_2 structure and may improve both charge transport and long-term stability.[27,28] However, the synthesis of single-crystalline large-area Na-MnO_2 has been lacking so far.

In this study, we report the synthesis of Na^+-intercalated ultra-thin layered MnO_2 nanosheets *via* a molten-salt-assisted solid-state process, a technique that offers superior crystalline quality and spontaneous Na^+ incorporation. We examine their structural properties and perform electrical measurements to illustrate their potential in ionic charge transport. The distinctive layered structure of single-crystalline Na-MnO_2 enables the efficient movement of ions when subjected to an electric field. Our research underscores the essential influence of ambient moisture on ionic mobility, and we illustrate the integration of this material into two-terminal devices to replicate synaptic functions. These results show that Na-MnO_2 can be considered for applications beyond batteries and supercapacitors. Moreover, Na-MnO_2 and K-MnO_2 devices can be used in conjunction to create functional devices.

2. Results and discussion

2.1. Na-MnO_2 synthesis and characterization

Na-MnO_2 crystal synthesis procedures were developed using the real-time optical chemical vapor deposition (RTO-CVD) method. Details of the RTO-CVD method can be found in our previously published studies.[19,29] The molten salt has dual functions: acting as both the reaction medium and ion source, facilitating the growth of high-quality, single-crystalline materials and enabling spontaneous ion intercalation during crystal formation. This method overcomes the limitations of vapor-phase- and solution-based techniques, allowing for the growth of large-area, defect-free materials with superior ionic mobility.[23–25] The formation of Na-MnO_2 involves melting a mixture of the metal oxide precursor (MnO_2 powder) and sodium salt (NaI powder) on a c-cut sapphire substrate to promote substrate-directed growth. Prior to use, the sapphire substrate was subjected to ultrasonic cleaning in acetone, isopropanol, and deionized water, after which it was dried using a high-purity N_2 spray gun. The NaI and MnO_2 powders were milled together into a fine powder of 3 : 1 ratio, and then a few granules were dispersed on the growth substrate for the molten-salt-assisted solid-state reaction, which was loaded onto a substrate heater, as schematically illustrated in Fig. 1a. The temperature was ramped to 670 °C at a rate of 25 °C per minute under ambient conditions. Once the target temperature was reached, nanosheets with the desired size and thickness formed within 10 minutes. The growth process was completed by allowing the substrate heater to cool naturally, and the samples were removed once they reached room temperature.

Fig. 1b shows the schematic representation of the layered MnO_2 crystals co-intercalated with Na^+ ions and water molecules. This material consists of sheets made up of [MnO_6] octahedra that share edges, creating pathways for the movement of Na^+ ions between them.[8,16] To characterize the synthesized crystals, we used Raman spectroscopy, X-ray diffraction (XRD), X-ray photoelectron spectroscopy (XPS), energy dispersive X-ray spectroscopy (EDX), and high-resolution transmission electron microscopy (HR-TEM) along with selected area electron diffraction (SAED) measurements on the samples. Optical, scanning electron, and atomic force microscopy techniques were employed to image crystals. Fig. 1c shows the optical micrograph of typical Na-MnO_2 nanosheets synthesized on a c-cut sapphire substrate. As illustrated in Fig. 1d, atomic force microscopy (AFM) height trace maps of the ultra-thin Na-MnO_2 reveal a 2.8 nm thick crystal with overgrowth of two atomic layers, considering that the distance between MnO_2 sheets is ~0.7 nm.[8,10,30,31] The nanosheets can grow as large as several tens of micrometers with uniformity across the crystal scale. Fig. S1† demonstrates another crystal typically possessing a hexagonal-shaped morphology with sharp edges and a thickness of 4.2 nm.

XRD results exhibit two strong peaks located at 12.6 and 25.2° corresponding to the (001) and (002) planes and they matched well with the JCPDS 00-043-1456 data card (Fig. 2a) for δ-MnO_2. The interlayer spacing we obtained from our measurements corresponds to 7.0 Å, which is slightly lower than the interlamellar spacing reported in the data card (7.1 Å).[22,30] Fig. 2b shows the SAED pattern indexed for the [001] zone axis of the crystal. The six-fold symmetric arrangement of the diffraction pattern reveals the single-crystalline nature of the nanosheets. Intriguingly, supercell reflections are visible in the SAED pattern. We consider that these reflections

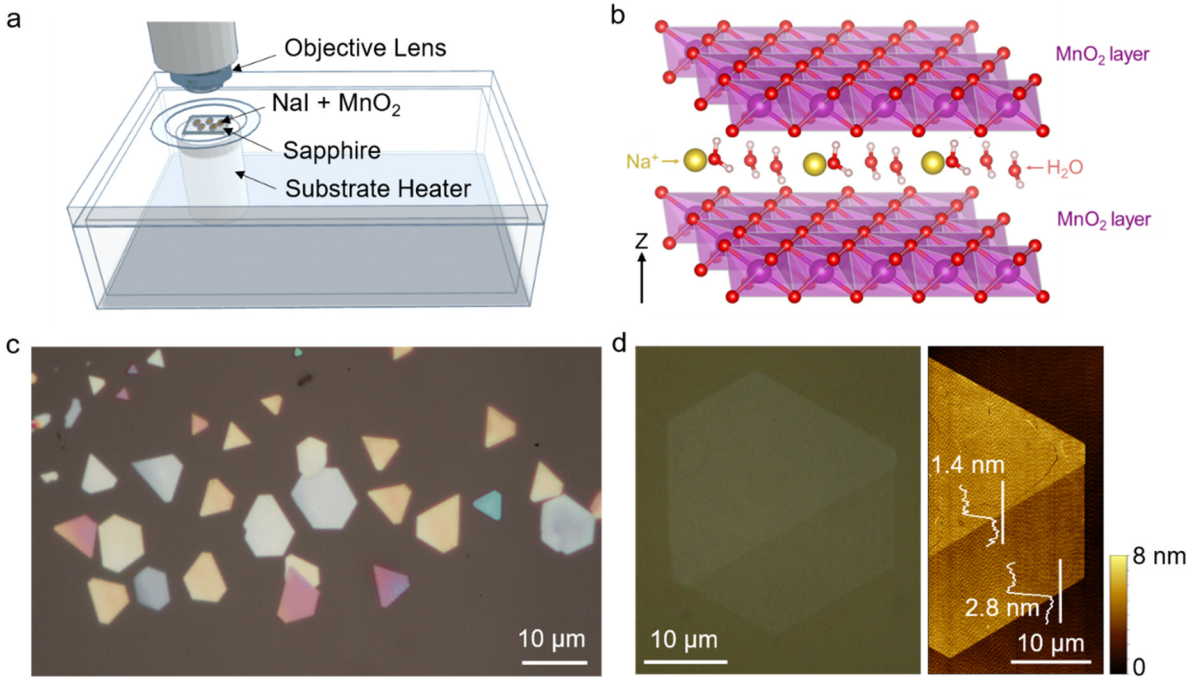

Fig. 1 (a) Schematic illustration of the growth of Na-MnO_2 crystals on a sapphire substrate. (b) Representative schematic of layered Na-MnO_2 crystals spontaneously intercalated with sodium ions during the growth. (c) Optical microscopy image of 2D Na-MnO_2 crystals on a sapphire substrate. (d) Optical observation of a 2D Na-MnO_2 crystal and the corresponding AFM image and height profile.

are from the interlayer Na and H_2O, as clarified later. Larger tilt angles with respect to the [001] zone axis show a better view of the supercell reflections due to the ordered distribution of interlayer cations (Fig. S2†). The inset shows the corresponding HR-TEM image. The crystalline spacing of 0.24 nm corresponds to the (11–1) plane, which perfectly agrees with the XRD data card. To qualitatively confirm the uniformity of the material, EDX spectra were collected on the TEM sample, which indicate a uniform distribution of Na, Mn, and O throughout the nanosheet (Fig. 2c).

XPS analysis also reveals the presence of Na 1s and Mn 2p peaks, which closely align with previously reported values[22,31–33] (Fig. 2d). The peak located at 1072.3 eV for Na 1s indicates the presence of Na^+ in the crystal. The core-level spectrum of Mn 2p exhibits two distinct peaks, Mn $2p_{3/2}$ and Mn $2p_{1/2}$, located at energy levels of 643.3 eV and 654.9 eV, respectively. The observed spin–orbit distance between the two Mn 2p peaks is 11.6, confirming the existence of the MnO_2 phase.[33] The observed splitting and broadening of the spectral lines in the Mn 2p spectrum point towards the existence of multiple oxidation states for manganese.[34,35] This observation is further reinforced by the binding energy difference (ΔE) of Mn 3s multiplet splitting, which is commonly used to qualitatively assess the oxidation state of Mn.[13,36] The measured ΔE value of approximately 5.1 eV confirms the presence of a mixed oxidation state (~+3.3) in the synthesized Na-MnO_2[34,37] (Fig. S3†). Upon Na^+ ion intercalation, some of the Mn^{4+} cations reduce to Mn^{3+} to counterbalance the charge in the whole structure.[8] The unstable high-spin Mn^{3+} in a degenerate electronic state undergoes geometrical distortion to form a system of lower symmetry, leading to the elongation of the [MnO_6] octahedron along the *z*-axis and volume expansion. This causes the transformation of the lattice structure from a hexagonal to an orthorhombic structure.[9,16,38] Further intercalation can induce a structural transition to monoclinic, which is in good agreement with the XRD result and previously reported literature.[11,16] Although there is a strong O 1s peak present in the spectra, it is dominated by the signal from the sapphire substrate.[39] The other peak located at 532.2 eV corresponds to the H–O–H bond,[17,33] which confirms that water molecules exist in the layered structure.

The aforementioned characterization studies suggest the successful intrinsic intercalation of Na^+ ions into δ-MnO_2 during the crystal synthesis *via* a molten-salt-assisted CVD approach, paving the way for further exploration of intercalated MnO_2 materials with tailored properties.

2.2. Interlamellar water intercalation

An important characteristic of the Na-MnO_2 crystals is their inherent ability to spontaneously incorporate ambient moisture between the layers, resulting in the formation of a hydration layer.[16] To investigate this phenomenon, we performed temperature-dependent Raman spectroscopy on the as-grown Na-MnO_2 sheets under 532 nm excitation (Fig. 3a). Based on group theoretical calculations, it is predicted that the layered MnO_2 exhibits a total of 9 Raman-active modes,[8] as experimentally characterized in Fig. 3a (spectrum labeled 'before heating'). The presence of all predicted modes suggests

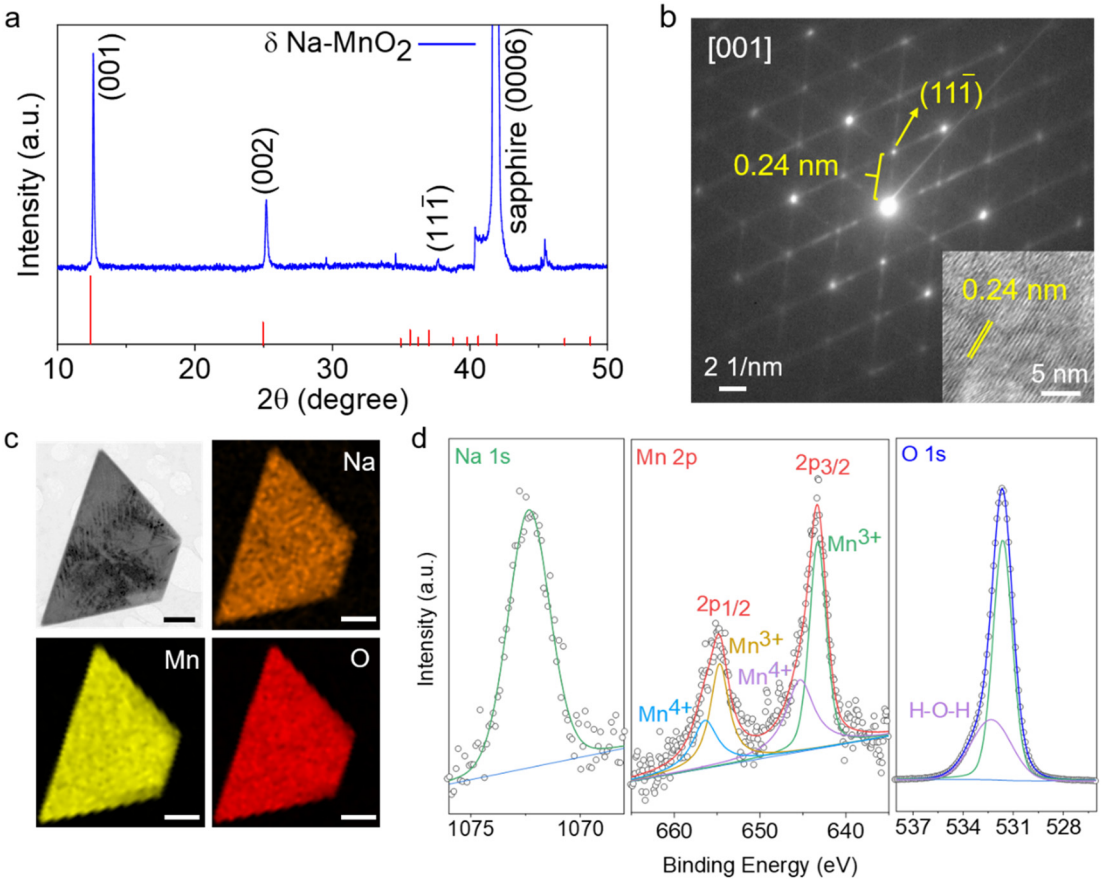

Fig. 2 (a) XRD θ–2θ scan of the Na-MnO_2 crystals at room temperature. The red lines indicate the peak positions in the JCPDS-00-043-1456 data card. (b) SAED pattern indexed along the [001] zone axis. The inset shows the HRTEM image of the crystal with an interplanar spacing of 0.24 nm. (c) EDX maps of Na, Mn, and O elements. The scale bar is 1 μm. (d) XPS core-level regions of Na 1s, Mn 2p, and O 1s, respectively.

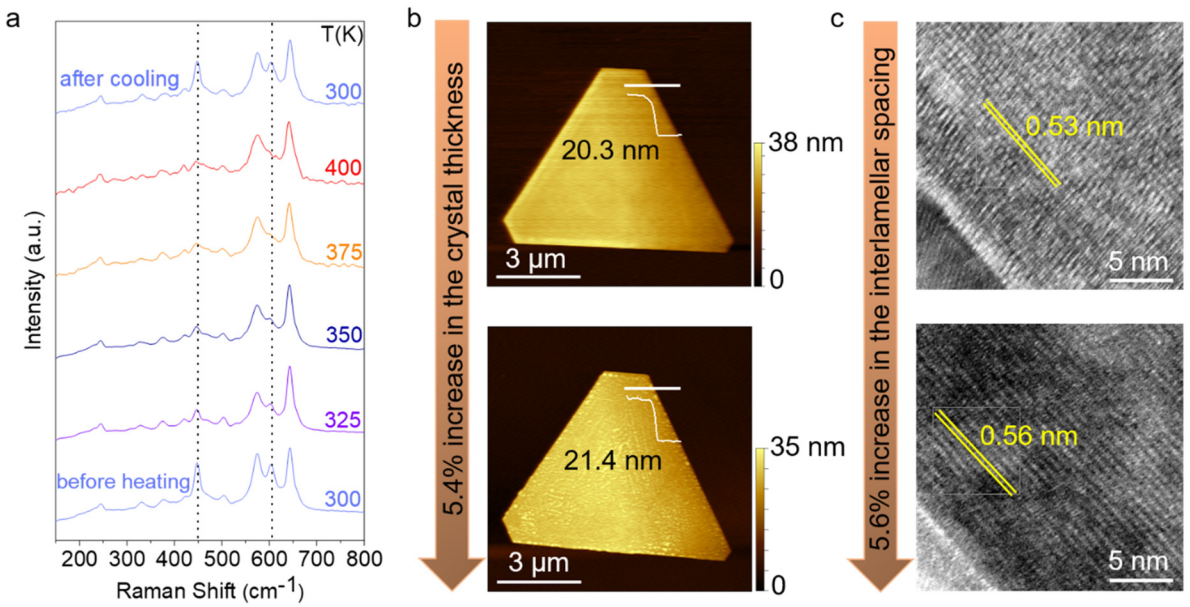

Fig. 3 (a) Raman spectra recorded under ambient conditions at various temperatures. The dashed lines mark the location of the peaks at 448 and 603 cm^{-1}. (b) AFM scans and (c) HR-TEM images of the crystal before and after 15 minutes of water immersion. The height difference complies with the increase in interlamellar spacing.

the high crystallinity of the synthesized Na-MnO_2 crystals. There are three main vibrational features located at 448, 575, and 643 cm^{-1} corresponding to the out-of-plane asymmetric bonding vibration of Mn–O or wagging vibration,[40] Mn–O symmetric stretching vibration along the [MnO_6] octahedral sheets, and Mn–O symmetric stretching vibration along the *c*-axis,[8,16,38,41,42] respectively. Based on these observed vibrational characteristics, it can be inferred that the obtained MnO_2 possesses a layered structure consistent with the birnessite type.

The Raman spectra found in the literature often lack the 603 cm^{-1} vibration mode due to the broadening of Raman features caused by the disorder present in the synthesized crystals using the aforementioned methods.[8,19] This peak is ascribed to the out-of-plane symmetric bending vibration of Mn–O or twisting vibration. Other peaks located at low wavenumbers are associated with translations of the interlayer Na^+ ions and water molecules.[8,11,16] As the temperature increases, the intensity of peaks located at 448 and 603 cm^{-1} notably decreases, attributed to the out-of-plane Mn–O vibrational modes. Upon cooling down to room temperature, the pristine spectrum is obtained intriguingly, indicating the absorption of water molecules from ambient moisture. Similar observations were reported for ultra-thin K-MnO_2 crystals, where temperature-dependent XRD measurements demonstrated a reduction in interlayer spacing.[19] This suggests that as the temperature increases, water molecules within the crystal structure are expelled.

To understand the effect of water intake on the interlayer spacing of Na-MnO_2, we conducted morphological analysis on the as-grown nanoflakes using AFM and TEM, both before and after a 15-minute immersion period in water. The AFM height profiles obtained along the white lines indicate a 5.4 ± 0.2% increase in nanoflake thickness (Fig. 3b). Cracks visible in certain crystals after elongated water immersion are a signature of the significant interlayer spacing change of the material. Cross-sectional TEM images further confirmed the layered structure of the crystals. Fig. 3c illustrates a comparison between the cross-sectional TEM images of a Na-MnO_2 sample immersed in water for 15 minutes and a pristine sample, revealing a 5.6 ± 0.3% increase in interlamellar spacing after water immersion. These values align closely, confirming the consistency between the AFM and TEM measurements. The hydration layer plays an important role in ionic charge transport, resulting from the change in the interlayer spacing of birnessite.[13]

2.3. Electrical measurements

Spontaneously ion intercalated δ-MnO_2 exhibits peculiar electrical properties thanks to the ionic charge transport. The ionic charge transport in solid electrolytes is a slow process compared to the electronic charge transport. Moreover, the ionic motion affects the layered material's interlayer spacing and local electrostatics. As a result, strong hysteresis is observed and this can be useful in mimicking biological neurons. Two-terminal devices were fabricated using standard optical lithography methods, followed by Cr/Au deposition. Current–voltage (*I–V*) measurement was performed under ambient conditions to characterize the electrical response of the crystals (Fig. 4a).

A wide hysteresis window was observed in the *I–V* curves, likely due to the slow movement of ions from the contacts into the material and the separation of water and sodium ions within it. Starting from 0 V and increasing the positive voltage, the device maintained a low resistance state (LRS) up to 10 V, where negative differential resistance (NDR) appeared. Within the NDR region, the resistance transitioned from the LRS to a high resistance state (HRS). The device remained in this HRS as the voltage was reduced from 10 V back to 0 V. Similar behavior was observed during the negative voltage sweep. After the *I–V* curve measurement was completed and returned to 0 V, the device stayed in its HRS. This hysteresis behavior suggests that the device can "remember" the history of applied voltages. Endurance testing over eight consecutive cycles, as shown in Fig. S4,† at a read voltage of around ±6 V—where the maximum LRS/HRS ratio occurs—demonstrates reliable switching between resistance states. This consistent switching highlights the potential of Na-MnO_2 nanosheets for memory-switching applications.

To ensure consistency and reliability across various devices, the device-to-device (D2D) variation was examined using 10 different devices. The *I–V* characteristics exhibited comparable hysteresis windows across the devices (Fig. S5a†). Furthermore, the statistical distributions of current values at the LRS and HRS at a read voltage of ±5 V are presented (Fig. S5b†). We consider that D2D variation is primarily due to differences in the thickness of the crystals used in device fabrication.

To determine the dominant charge carrier type, we conducted voltage–time (*V–t*) measurements under constant current, as depicted in Fig. 4b. Applying a constant current resulted in a voltage increase across the contacts following an exponential trend. Similarly, when the current was removed, the voltage across the contacts exhibited exponential decay. In both cases, the experimental data aligned perfectly with the empirical formula $V(t) = V_0 + V_1 e^{-t/\lambda}$, where V_0 and V_1 represent the fitting parameters and λ represents the time constant for the exponential decay function. The calculated λ values are in the order of several seconds. In a device with purely electronic conductivity, λ would be less than a millisecond. However, for a mixed ionic–electronic conductor, λ may last for even a few minutes due to the relatively sluggish movement of ions, leading to the accumulation of voltage across the contacts. These observations provide evidence for the mixed conductivity nature of charge transport in Na-MnO_2 devices. Similar mixed ion–electron conduction mechanisms have been reported in other oxide-based systems.[43]

To further investigate the mechanisms causing hysteresis, we visually monitored the changes in the device during biasing and conducted Raman spectroscopy. Fig. 4c illustrates a device with gold electrodes, where one electrode was fixed to the ground while a constant voltage was applied through the other electrode. A series of optical microscopy images were

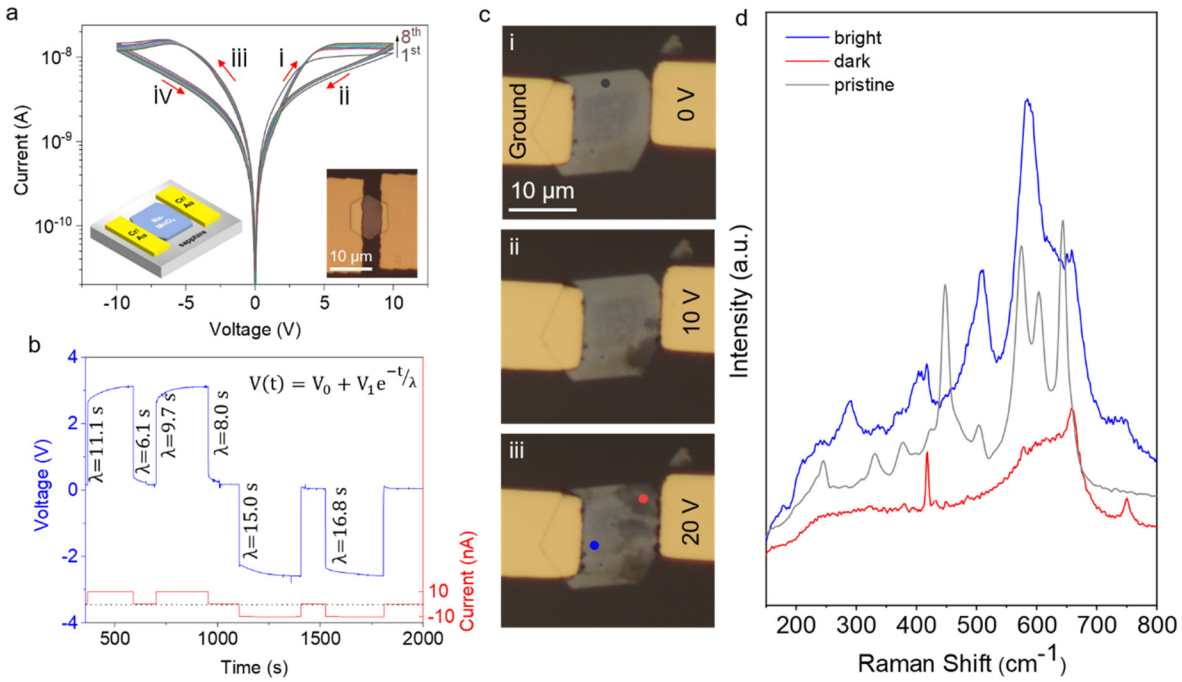

Fig. 4 (a) Eight consecutive *I*–*V* cycles taken from a device. The real and schematic images of an exemplary gold contact device are shown in the inset. (b) *V*–*t* scan under constant current conditions demonstrating an exponential decay in the voltage response across the electrodes. λ is the time constant in the exponential function. The red line shows the current applied at various times. (c) Series of optical microscopy images taken during biasing of a two-terminal device of Na-MnO_2. (d) Raman spectra recorded at the positions indicated in (c), the gray (pristine) point marked in (i), and the red and blue points marked in (iii).

captured during the biasing process, revealing significant optical changes in the crystal. The initial image depicts the state just before applying a 10 V bias (Fig. 4ci), and subsequent images showcase the evolution of optical contrast within the crystal. As the bias is increased to 20 V (Fig. 4ciii), the optical contrast near the biased electrode becomes more pronounced than that of the pristine crystal.

As discussed earlier, the pristine layered MnO_2 reveals a total of 9 Raman-active modes,[8] as shown in Fig. 4d (gray spectrum). Analysis of the Raman spectrum obtained from the dark contrast region suggests the absence of vibrational modes at low wavenumbers, indicative of no translations of interlayer Na^+ ions and water molecules. This distinctly different Raman spectrum from that of the bright contrast region hints at the formation of spinel Mn_3O_4, which resulted from the separation of the hydration layer around the Na^+ ions.[8,19] The migration of ions and the intercalation/deintercalation of water from the ambient environment in Na-MnO_2 lead to reversible phase transitions in the crystal structure, alternating between layered and spinel phases. These transitions are accompanied by variations in ionic content, resulting in changes in optical contrast. The above results indicate that the presence of Na^+ ions and water molecules significantly strengthens the stability of the layered structure, acting as sturdy pillars to support its integrity, confirmed by previously reported literature.[31,44,45]

Furthermore, devices subjected to *I*–*V* cycling in a vacuum exhibited reduced hysteresis (Fig. S6b†). Additionally, measurements were performed under ambient conditions after immersing the device in water for 30 seconds, where the relative humidity can be considered equivalent to 100%. A significant enhancement in both the electrical response and hysteresis window was observed (Fig. S6c†). This supports the idea that Na^+ ions are more readily reintegrated in the presence of moisture.

2.4. Synapse-like response of Na-MnO_2 devices

Artificial synapses can be created using a variety of materials, enabling the construction of neuromorphic devices capable of performing tasks such as image recognition and natural language processing.[46,47] One promising material for artificial synapses is spontaneously ion intercalated δ-MnO_2, which has demonstrated synaptic plasticity—the ability to modify its conductance in response to repeated electrical pulses.[7,19,48] To demonstrate the neuromorphic capabilities of Na-MnO_2-based devices, the short-term potentiation (STP) of the devices was evaluated (Fig. 5a). Two pulses, each with a temporal width of 0.1 s and a pulsing voltage of 5 V, separated by 1.5 s, caused a gradual change in the device's conductance, that is, facilitation of the synapse. The read voltage was set to 1 V to prevent changes in the resistance state of the device.

The resistive switching in Na-MnO_2 is governed by Na^+ ion migration and Mn redox interactions, which enable gradual conductance modulation. This mechanism differs from purely filamentary memristors, where resistance switching is typically

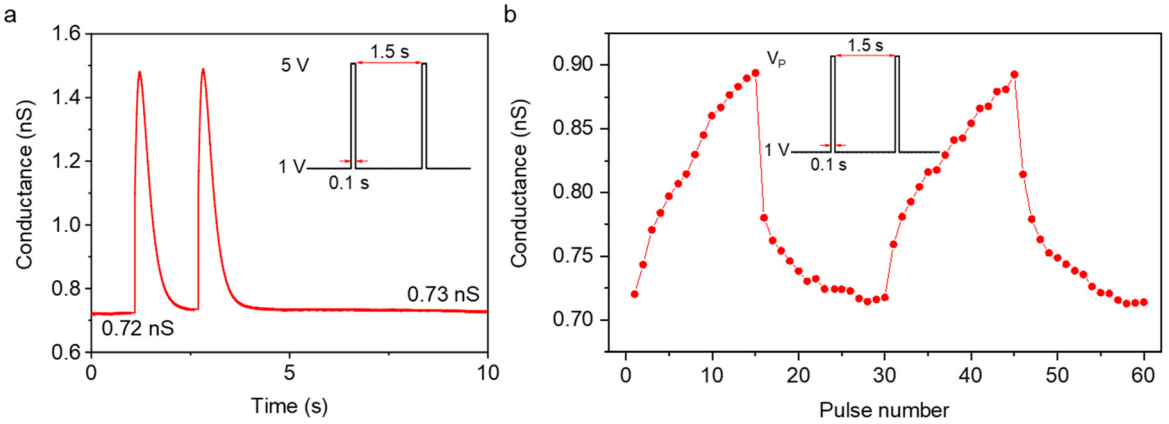

Fig. 5 (a) Short-term potentiation (STP) of the device showing a gradual change in the conductance of the Na-MnO_2 device. The conductance value is read with 1 V. Two spikes 1.5 s apart at 5 V with 0.1 s temporal width are sent to induce the change. (b) Long-term potentiation (LTP) and depression (LTD). LTP and LTD are shown with pulse voltages (V_P) of 5 and −5 V, respectively, while the read voltage is 1 V. Pulses are separated by 1.5 s and last for 0.1 s.

abrupt.[49,50] Similar to other ion-based neuromorphic materials, such as WO_x[51] and K-MnO_2,[19] the reported devices exhibit longer switching times of approximately 100 ms and estimated energy per spike of 0.5 nJ. The energy per spike values are within the expected range for mixed ionic–electronic conduction systems, yet significantly larger than those of filamentary memristors. We acknowledge that the operating voltage (~4 V) of the device is higher than those of some oxide-based memristors, and further optimization, such as reducing the device channel length and improving ionic mobility, may lower the overall energy dissipation. However, given its ability to achieve gradual synaptic plasticity, ultrathin Na-MnO_2 remains a relevant material for neuromorphic computing.

Long-term potentiation (LTP) and depression (LTD) are crucial mechanisms in synaptic plasticity, commonly associated with learning and memory in biological systems. These mechanisms mimic the brain's ability to strengthen or weaken synaptic connections.[47,48] LTP and LTD effects are also observed in Na-MnO_2 devices (Fig. 5b). The conductance of these devices can be gradually modified by applying a series of voltage pulses. The high resistance and low resistance states can be repeatedly achieved upon cycling the devices (Fig. S4†). We successfully developed a device using a single Na-birnessite nanosheet, positioning this material as a promising candidate for neuromorphic computing applications.

3. Conclusion

In summary, we have successfully synthesized Na^+-intercalated ultra-thin MnO_2 nanosheets using real-time chemical vapor deposition *via* the molten-salt-assisted synthesis method, offering a novel route for producing single-crystalline, layered materials with intrinsic ionic charge transport properties. Our structural and electrochemical analysis demonstrates that this method not only yields highly ordered δ-MnO_2 but also promotes spontaneous Na^+ intercalation, which is critical for enhanced ionic mobility and stability. The ambient moisture was found to play a pivotal role in modulating ion transport, further optimizing the electrochemical performance of these nanosheets. The distinctive layered architecture of Na-MnO_2 enables efficient electron and ion movement under an electric field, which we have shown to be advantageous for neuromorphic applications. The results obtained from the two-terminal devices suggest that this material can mimic synaptic behavior, paving the way for its use in ion-mediated charge transport systems. Overall, the insights gained from this study provide a foundation for further exploration of Na^+-intercalated MnO_2 in diverse fields, including neuromorphic computing, beyond traditional energy storage applications.

Author contributions

AP performed the crystal synthesis and characterization with the help of AAS. DP, HMS, and EY performed device fabrication and aided AP, MR, and UB in electrical measurements. OO performed AFM scans. TSK conceded the project and guided the experiments. AP and TSK wrote the manuscript with the contributions of all authors.

Data availability

The data that support the plots within this paper and other findings of this study are available from the corresponding authors upon request. Some of the data supporting this article have been included in the ESI.†

Conflicts of interest

There are no conflicts to declare.

Acknowledgements

TSK acknowledges funding from TUBITAK under grant #120N885. AP and AAS were also partially supported by TUBITAK grant #121F366 during the course of the study.

References

1 X. Xu, Y. Chen, P. Liu, H. Luo, Z. Li, D. Li, H. Wang, X. Song, J. Wu, X. Zhou and T. Zhai, *Nat. Commun.*, 2024, **15**, 4368.
2 C. Liu, H. Chen, S. Wang, Q. Liu, Y. G. Jiang, D. W. Zhang, M. Liu and P. Zhou, *Nat. Nanotechnol.*, 2020, **15**, 545–557.
3 Y. Li, H. Yan, B. Xu, L. Zhen and C. Y. Xu, *Adv. Mater.*, 2021, **33**, e2000581.
4 J. Zhang, A. Yang, X. Wu, J. van de Groep, P. Tang, S. Li, B. Liu, F. Shi, J. Wan, Q. Li, Y. Sun, Z. Lu, X. Zheng, G. Zhou, C. L. Wu, S. C. Zhang, M. L. Brongersma, J. Li and Y. Cui, *Nat. Commun.*, 2018, **9**, 5289.
5 Y. Wu, J. Wang, Y. Li, J. Zhou, B. Y. Wang, A. Yang, L. W. Wang, H. Y. Hwang and Y. Cui, *Nat. Commun.*, 2022, **13**, 3008.
6 L. Tian, H. Qiao, Z. Huang and X. Qi, *Cryst. Res. Technol.*, 2021, **56**, 2000165.
7 X. Zhu, D. Li, X. Liang and W. D. Lu, *Nat. Mater.*, 2019, **18**, 141–148.
8 C. Julien, *Solid State Ionics*, 2003, **159**, 345–356.
9 K. P. Lucht and J. L. Mendoza-Cortes, *J. Phys. Chem. C*, 2015, **119**, 22838–22846.
10 X. Shan, F. Guo, D. S. Charles, Z. Lebens-Higgins, S. Abdel Razek, J. Wu, W. Xu, W. Yang, K. L. Page, J. C. Neuefeind, M. Feygenson, L. F. J. Piper and X. Teng, *Nat. Commun.*, 2019, **10**, 4975.
11 J. E. Post, D. A. McKeown and P. J. Heaney, *Am. Mineral.*, 2021, **106**, 351–366.
12 K. W. Nam, S. Kim, S. Lee, M. Salama, I. Shterenberg, Y. Gofer, J. S. Kim, E. Yang, C. S. Park, J. S. Kim, S. S. Lee, W. S. Chang, S. G. Doo, Y. N. Jo, Y. Jung, D. Aurbach and J. W. Choi, *Nano Lett.*, 2015, **15**, 4071–4079.
13 B. Li, Y. Chu, B. Xie, Y. Sun, L. Zhang, H. Zhao, L. Zhao, P.-F. Liu and J. He, *J. Mater. Chem. A*, 2023, **11**, 2133–2144.
14 J. Wang, G. Zhang and P. Zhang, *J. Mater. Chem. A*, 2017, **5**, 5719–5725.
15 M. B. Ghasemian, M. Mayyas, S. A. Idrus-Saidi, M. A. Jamal, J. Yang, S. S. Mofarah, E. Adabifiroozjaei, J. Tang, N. Syed, A. P. O'Mullane, T. Daeneke and K. Kalantar-Zadeh, *Adv. Funct. Mater.*, 2019, **29**, 1901649.
16 G. Brugnetti, C. Triolo, A. Massaro, I. Ostroman, N. Pianta, C. Ferrara, D. Sheptyakov, A. B. Munoz-Garcia, M. Pavone, S. Santangelo and R. Ruffo, *Chem. Mater.*, 2023, **35**, 8440–8454.
17 G. U. Kamble, A. V. Takaloo, A. M. Teli, Y. J. Kim, P. Sonar, T. D. Dongale, D.-k. Kim and T. W. Kim, *J. Alloys Compd.*, 2021, **872**, 159653.
18 S. Li, M. Zhao, D. Zhang and X. Wu, *Cryst. Growth Des.*, 2023, **23**, 8156–8162.
19 H. R. Rasouli, J. Kim, N. Mehmood, A. Sheraz, M. K. Jo, S. Song, K. Kang and T. S. Kasirga, *Nano Lett.*, 2021, **21**, 3997–4005.
20 B. R. Chen, W. Sun, D. A. Kitchaev, J. S. Mangum, V. Thampy, L. M. Garten, D. S. Ginley, B. P. Gorman, K. H. Stone, G. Ceder, M. F. Toney and L. T. Schelhas, *Nat. Commun.*, 2018, **9**, 2553.
21 D. A. Kitchaev, S. T. Dacek, W. Sun and G. Ceder, *J. Am. Chem. Soc.*, 2017, **139**, 2672–2681.
22 Y. Liu, S. Zhu, Z. Zhang, Q. Sun, C. Wu, W. Gong, L. Kang and Y. Yang, *J. Alloys Compd.*, 2023, **957**, 170362.
23 Q. Na, G. Zhang, J. Wang, Y. Zhang, R. Li, J. Wang, C. Wang and J. Zhang, *Mater. Charact.*, 2024, **217**, 114412.
24 Q. Sun, S. Zhu, Z. Shen, Y. Liu, C. Wu, L. Kang and Y. Yang, *Mater. Today Chem.*, 2023, **29**, 101419.
25 G. Ding, M. Yao, J. Li, T. Yang, Y. Zhang, K. Liu, X. Huang, Z. Wu, J. Chen, Z. Wu, J. Du, C. Rong, Q. Liu, W. Zhang and F. Cheng, *Adv. Energy Mater.*, 2023, **13**, 2300407.
26 C. R. Rose and A. Konnerth, *J. Neurosci.*, 2001, **21**, 4207–4214.
27 R. D. Shannon, *Acta Crystallogr., Sect. A*, 1976, **32**, 751–767.
28 Y. Ding, W. Xue, K. Chen, C. Yang, Q. Feng, D. Zheng, W. Xu, F. Wang and X. Lu, *Nanomaterials*, 2023, **13**(6), 1075.
29 H. R. Rasouli, N. Mehmood, O. Cakiroglu and T. S. Kasirga, *Nanoscale*, 2019, **11**, 7317–7323.
30 J. Zhou, L. Yu, M. Sun, S. Yang, F. Ye, J. He and Z. Hao, *Ind. Eng. Chem. Res.*, 2013, **52**, 9586–9593.
31 D. Wang, L. Wang, G. Liang, H. Li, Z. Liu, Z. Tang, J. Liang and C. Zhi, *ACS Nano*, 2019, **13**, 10643–10652.
32 X. Zhang, P. Yu, H. Zhang, D. Zhang, X. Sun and Y. Ma, *Electrochim. Acta*, 2013, **89**, 523–529.
33 Q. Xie, G. Cheng, T. Xue, L. Huang, S. Chen, Y. Sun, M. Sun, H. Wang and L. Yu, *Mater. Today Energy*, 2022, **24**, 100934.
34 T. B. M. Toupin and D. Belanger, *Chem. Mater. Lett.*, 2002, **14**, 3946–3952.
35 S. Dang, Y. Wen, T. Qin, J. Hao, H. Li, J. Huang, D. Yan, G. Cao and S. Peng, *Chem. Eng. J.*, 2020, **396**, 125342.
36 T. Gao, P. Norby, F. Krumeich, H. Okamoto, R. Nesper and H. Fjellvåg, *J. Phys. Chem. C*, 2010, **114**, 922–928.
37 E. S. Ilton, J. E. Post, P. J. Heaney, F. T. Ling and S. N. Kerisit, *Appl. Surf. Sci.*, 2016, **366**, 475–485.
38 S. Q. Wang, B. Zhang, R. H. Qiao, Y. W. Luo, X. M. Luo and G. P. Zhang, *ACS Appl. Electron. Mater.*, 2023, **5**, 4836–4845.
39 H. R. Rasouli, N. Mehmood, O. Çakiroglu, E. C. Sürmeli and T. S. Kasirga, *Phys. Rev. B: Condens. Matter Mater. Phys.*, 2019, **100**, 161107.
40 C. M. Julien, M. Massot and C. Poinsignon, *Spectrochim. Acta, Part A*, 2004, **60**, 689–700.
41 M. Tu, H. Lu, S. Luo, H. Peng, S. Li, Y. Ke, S. Yuan, W. Huang, W. Jie and J. Hao, *ACS Appl. Mater. Interfaces*, 2020, **12**, 24133–24140.
42 M. A. Belal, R. Yousry, G. Taulo, A. A. AbdelHamid, A. E. Rashed and A. A. El-Moneim, *ACS Appl. Mater. Interfaces*, 2023, **15**, 53632–53643.

43 Y. Aoki, C. Wiemann, V. Feyer, H. S. Kim, C. M. Schneider, H. Ill-Yoo and M. Martin, *Nat. Commun.*, 2014, **5**, 3473.
44 S. Zhu, Y. Wang, J. Zhang, J. Sheng, F. Yang, M. Wang, J. Ni, H. Jiang and Y. Li, *Energy Environ. Mater.*, 2022, **6**, e12382.
45 C.-Y. Tsai, T.-S. Su, T.-C. Wei and M.-S. Wu, *Electrochim. Acta*, 2022, **430**, 141107.
46 W. Ahn, H. B. Jeong, J. Oh, W. Hong, J. H. Cha, H. Y. Jeong and S. Y. Choi, *Small*, 2023, **19**, e2300223.
47 J. H. Baek, I. H. Im, E.-M. Hur, J. Park, J. Lim, S. Kim, K. Kang, S. Y. Kim, J. Y. Song and H. W. Jang, *Mater. Res. Bull.*, 2024, **176**, 112803.
48 J. Zhu, Y. Yang, R. Jia, Z. Liang, W. Zhu, Z. U. Rehman, L. Bao, X. Zhang, Y. Cai, L. Song and R. Huang, *Adv. Mater.*, 2018, **30**, e1800195.
49 Y. Zhang, G. Q. Mao, X. Zhao, Y. Li, M. Zhang, Z. Wu, W. Wu, H. Sun, Y. Guo, L. Wang, X. Zhang, Q. Liu, H. Lv, K. H. Xue, G. Xu, X. Miao, S. Long and M. Liu, *Nat. Commun.*, 2021, **12**, 7232.
50 S. J. Yang, Y.-R. Jeon, D. Kim, S. Mohan, S. Kutagulla, M. Disiena, S. K. Banerjee and D. Akinwande, *npj 2D Mater. Appl.*, 2025, **9**, 9.
51 Y. Lin, F. Meng, T. Zeng, Q. Zhang, Z. Wang, Y. Cheng, X. Zhao, L. Gu, H. Xu and Y. Liu, *Adv. Funct. Mater.*, 2023, **33**, 2302787.